Apparent apertures from ground penetrating radar data and their relation to heterogeneous aperture fields

A. Shakas and N. Linde

Applied and Environmental Geophysics Group, Institute of Earth Sciences, University of Lausanne, 1015 *Lausanne, Switzerland.*
E-mail: alexis.shakas@unil.ch

SUMMARY

Considering fractures with heterogeneous aperture distributions, we explore the reliability of constant-aperture estimates derived from ground penetrating radar (GPR) reflection data. We generate geostatistical fracture aperture realizations that are characterized by the same mean-aperture and variance, but different Hurst exponents and cut-off lengths. For each of the 16 classes of heterogeneity considered, we generate 1000 fracture realizations from which we compute GPR reflection data using our recent effective-dipole forward model. We then use each (noise-contaminated) data set individually to invert for a single 'apparent' aperture, that is, we assume that the fracture aperture is homogeneous. We find that the inferred 'apparent' apertures are only reliable when fracture heterogeneity is non-fractal (the Hurst exponent is close to 1) and the scale of the dominant aperture heterogeneities is larger than the first Fresnel zone. These results are a direct consequence of the nonlinear character of the thin-bed reflection coefficients. As fracture heterogeneity is ubiquitous and often fractal, our results suggest that robust field-based inference of fracture aperture can only be achieved by accounting for the nonlinear response of fracture heterogeneity on GPR data.

Key words: Fracture and flow; Electromagnetic theory; Ground penetrating radar; Fractals and multifractals; Numerical modelling.

1 INTRODUCTION

Rock fractures play an important role in many hydrogeological and geotechnical processes (e.g. National Research Council, Committee on Fracture Characterization and Fluid Flow 1996). For instance, fractures can act as conduits (or barriers) for fluid flow in petroleum and groundwater reservoirs. Hydraulically significant fractures play a determinant role in the transport of chemicals and their properties need to be known in order to determine suitable safety measures, such as in the design of a nuclear waste repository (Tsang *et al.* 2015). Moreover, fracture detection is important for rock-fall hazard assessment (e.g. Jeannin *et al.* 2006), safety inspection of buildings (e.g. Patriarca *et al.* 2011) and can even aid as a precursor for volcanic eruptions (Kilburn & Voight 1998). Therefore, the identification and characterization of rock fractures is arguably a fundamental problem in groundwater hydrology and applied geophysics. Nonetheless, this remains very challenging in practice as fracture properties often need to be deduced from indirect geophysical data or through hydrogeological experiments, such as tracer tests.

Rock fractures often have a material filling with highly contrasting electrical properties to the host rock, such as water-filled fractures in granite. Such a setting is ideal for ground penetrating radar (GPR) imaging since the strong property contrast—often both in terms of electrical permittivity and conductivity—makes it possible to detect, at high resolution, fractures with apertures that are

several orders of magnitude smaller than the dominant wavelength of the source wavelet (e.g. Grasmueck 1996). In the latter case, the interference of the source wavelet with the fracture walls results in a superposition of reflections (transmissions), such that no distinction can be made between the individual reflections (transmissions) arising from the two interfaces of the fracture. Below this limit, derived by Bradford & Deeds (2006) as $\frac{3}{4}$ of the dominant GPR signal-wavelength, fracture aperture has been classically estimated by invoking the thin-bed approximation.

The ability of GPR to image fractures has been studied both theoretically (Bradford & Deeds 2006; Deparis & Garambois 2008) and in controlled experiments (Grégoire & Hollender 2004; Tsoflias & Hoch 2006). Field studies have successfully imaged fractures in reflection (Dorn *et al.* 2012) and transmission (Tsoflias *et al.* 2004; Sassen & Everett 2009) mode. Furthermore, time-lapse imaging experiments have demonstrated the potential of GPR to dynamically image transport of electrically conductive tracers (Tsoflias *et al.* 2001; Day-Lewis *et al.* 2003; Talley *et al.* 2005; Tsoflias & Becker 2008; Dorn *et al.* 2011; Shakas *et al.* 2016). A recent study by Tsoflias *et al.* (2015) suggests that multipolarization GPR data can better constrain flow channelling, however, it is not always possible to obtain all components of the GPR signal (e.g. for conventional borehole GPR systems). Nevertheless, the challenge remains on how to effectively interpret the information content in the GPR signal to make reliable aperture estimates in the presence of fractures with heterogeneous properties (i.e. any fracture found

in a natural system). To date, virtually all GPR studies have relied on the implicit assumption of constant aperture and material properties over the first Fresnel zone.

The impracticability of fully numerical models, such as finite-difference time-domain (FDTD), to adequately simulate very thin and heterogeneous fractures is mainly related to discretization. Using the traditional FDTD approach, one would need to discretize a fracture with at least 10 nodes (e.g. 0.1 mm node spacing for a 1 mm aperture) to accurately capture the GPR source-wavelet interaction with the fracture filling. Assuming a 100 MHz dominant source-wavelength and a granitic host rock in a typical modelling domain (e.g. a cube that spans at least 10 m in each dimension) the FDTD model would require Maxwell's equations to be solved on 10^{14} nodes. Such a problem is extremely challenging (often impossible) to model numerically. Additionally, inadequate discretization, the introduction of slanted surfaces in the often-used Cartesian grid and the artificial imposition of boundaries in the modelling domain lead to unwanted numerical artefacts. These disadvantages can be overcome with alternative modelling tools, such as the Finite Element method (e.g. Mukherjee & Everett 2011), that can efficiently model fractures with the use of thin elements and mesh refinement, but has not been widely used in the GPR community.

An alternative approach to simulate GPR reflection and transmission in fractured rock is to use analytic solutions for thin-layer interference. Widess (1973) was the first to relate the effect of thin-bed (or thin-layer, as it was originally introduced) properties on geophysical data. In his classic article, Widess examined the reflective properties of a geological layer whose thickness is small compared to the incoming seismic wavelength. In the electromagnetic (EM) counterpart, the same response arises from solving Maxwell's equations on the boundaries of a thin-bed. This leads to the well-known optics phenomenon called 'thin-film interference' (e.g. Orfanidis 2002, Ch. 5). The resulting equations can be separated into transverse-electric (TE) and transverse-magnetic (TM) modes.

Several studies use the EM thin-bed reflection coefficients to model the GPR response. For example, Grégoire & Hollender (2004) invert for the electrical properties of a filling between two granitic blocks using GPR reflection data from a laboratory experiment, Deparis & Garambois (2008) use common offset GPR reflection data to invert for electrical properties and aperture of a single fracture, Tsoflias & Becker (2008) use multifrequency GPR to investigate the relationship between fracture aperture and fluid electrical conductivity, Sambuelli & Calzoni (2010) successfully model GPR reflections from a mm-thin fracture in a marble block and compare them with a controlled experiment and Sassen & Everett (2009) use polarimetric GPR transmission data to determine electrical properties and aperture of a single fracture. More recently, Babcock & Bradford (2015) use GPR reflection data to quantify electrical properties and thickness of thin and ultrathin non-aqueous-phase liquid layers and Grobbe & Slob (2016) couple the thin-bed reflection coefficients to simulate the seismo-electric effect. In all these studies, the analogy between a fracture and a thin-bed is made.

The validity of the EM thin-bed solution depends on two conditions: (1) that the incoming field arrives as a plane wave over the whole thin-bed interface and (2) that the thin-bed extends infinitely along the plane of incidence. Both assumptions are violated to varying extent in practice. Another basic disadvantage of the thin-bed approach is that the aperture (thickness) and electrical properties of the bed are constant. In reality, fracture aperture variations within a fracture span several orders of magnitude (e.g. Bonnet *et al.* 2001). Moreover, studies that utilize GPR to detect the presence of an elec-

trically conductive tracer in a fractured system are confronted with highly heterogeneous tracer distributions, and consequently electrical conductivity, in the involved fractures, that can lead to signal depolarization (Tsoflias *et al.* 2015).

Another way to solve the thin-bed interference problem relies on an analogy to the microscopic treatment of electromagnetic wave propagation in dielectric media. The analysis begins with the realization that optical phenomena, such as thin-bed interference, are in fact based on macroscopic (bulk) representations of the dielectric properties of a material that can be derived as space-time averages of a more fundamental microscopic treatment (Russakoff 1970). Microscopically, a dielectric is treated as a collection of discrete elements (electrons at the smallest scale) that can be polarized by the incoming field. For the typical frequencies used in GPR applications (MHz to GHz range), the dominant mechanism is molecular polarization in which polar molecules (such as water) rotate in response to the incoming field and then release energy during relaxation (e.g. Jol 2008, section 2.3). The collective sum of responses from all the polarizable elements exactly reproduces the (retarded) electromagnetic wave that one observes in dielectric media, which precisely reduces to the Fresnel equations on dielectric boundaries (Fearn *et al.* 1996) and accurately explains thin-bed interference (Lai *et al.* 2002).

We have recently presented how this analogy to the microscopic viewpoint can be used to efficiently simulate the electromagnetic response of a fracture of arbitrary properties, embedded within a homogeneous dielectric medium (Shakas & Linde 2015). Our approach, that we refer to as the effective-dipole method, consists of discretizing the fracture into a large collection of dipole elements. Each element radiates as an electric dipole that is modulated by the thin-bed reflection coefficients. Discretizing the fracture into elements provides two advantages: (1) we can account for the variation of the incoming field (intensity and orientation) along the fracture for a given antenna radiation pattern and (2) we can account for variations in electric and geometric properties of a finite-sized fracture (i.e. allow for heterogeneity in the fracture filling and aperture). Moreover, the effective-dipole method offers computation times that are several orders of magnitude smaller than FDTD simulations. A similar approach has been used by Michalski & Zheng (1990) to model radiation and scattering from perfectly conducting objects and later extended to magnetic dipoles in order to model underground unexploded ordnance by Shubitidze *et al.* (2002).

It is presently unclear if aperture estimation based on fully analytic forward models that rely on the thin-bed reflection coefficients is reliable in the presence of heterogeneous fracture properties. This question is addressed here by using our effective-dipole method, that offers the first opportunity to simulate realistic GPR responses from heterogeneous fractures. Initially, we confirm that the thin-bed forward model is reliable when considering a large enough and homogeneous fracture. Considering fractures with constant apertures, we demonstrate that aperture can be reliably estimated using a simple over-determined inversion scheme. We proceed by assigning heterogeneous fracture properties using the power spectrum method (a Fourier transform technique). We then demonstrate the ability of our effective-dipole method to reproduce 3-D FDTD simulations for a fracture with a heterogeneous conductivity distribution. After this, we use the effective-dipole method to simulate noise-contaminated GPR reflection data from fractures with highly heterogeneous aperture distributions. To accomplish this, we create 16 classes of geostatistical models that all share the same mean aperture and variance, but exhibit different Hurst exponents and cut-off lengths. The Hurst exponent and cut-off length define the trade-off between the fractal

nature (equal aperture heterogeneity present at all scales) and size of the largest aperture heterogeneity, respectively. Within each class, we evaluate 1000 fracture realizations. From the resulting data set, we infer the apparent constant-aperture of a homogeneous fracture whose GPR response, using the thin-bed forward model, best reproduces the data. These apertures are compared with spatial averaging weights derived from the sensitivity of the effective-dipole forward model for the given geometrical setup and a constant aperture fracture. Using these weights we obtain a weighted (mean) aperture, for each fracture realization, that we compare to the corresponding inferred (apparent) aperture. Based on this comparison, we present the conditions under which aperture heterogeneity leads to aperture estimates that are widely different from a linear average of the fracture aperture field.

2 METHODOLOGY AND THEORETICAL BACKGROUND

In this section, we first introduce the thin-bed forward model. We proceed by defining the modelling domain considered, with a single fracture present in a homogeneous rock matrix. We then describe the technique used to simulate heterogeneous fracture properties and use both FDTD and our effective-dipole method to simulate the GPR response for a fracture with a highly heterogeneous conductivity distribution. For all simulations, we use the same relative electric permittivity ($\epsilon_r = 9$) and electric conductivity ($\sigma = 0.001$ S m^{-1}) for the background matrix.

2.1 The thin-bed forward model

The thin-bed reflection coefficients can be derived from the macroscopic Maxwell's equations by considering an electromagnetic field impinging a layer with contrasting electrical properties to a background material (e.g. Orfanidis 2002, section 4.4). The same solutions are obtained by modelling the contrasting layers as a collection of dipoles and summing up their contribution (Lai *et al.* 2002). Both derivations rely on two basic assumptions: (1) that the incoming field strikes the layer with a constant (or periodic) angle, phase and amplitude everywhere and (2) that the layer has homogeneous properties and extends infinitely.

When these assumptions hold, the thin-bed reflection coefficients can be used to simulate GPR reflections resulting from a fracture with aperture a, through the following forward model:

$$\mathbf{E}_r(\mathbf{x}_s, \mathbf{x}_r, k_b, k_a, \theta) = \mathbf{E}_s(\mathbf{x}_s, k_b)\mathbf{R}_e(k_b, k_a, \theta)\mathbf{F}(*)\frac{e^{-ik_b x_r}}{x_r}, \quad (1)$$

where k_b (k_a) is the complex wavenumber $k = \frac{\omega}{c}\sqrt{\epsilon_r + \frac{i\sigma}{\omega}}$ in the background matrix (thin-bed) that depends on the angular frequency ω, relative electric permittivity ϵ_r and electric conductivity σ. Both materials are assumed to be non-magnetic and the speed of light in vacuum is $c \equiv 299792458$ m s^{-1}, $\mathbf{E}_r$ is the electric field measured at the receiver location and $\mathbf{E}_s$ is the electric field from an infinitesimal electric dipole source $\mathbf{p}$,

$$\mathbf{E}_s(\mathbf{x}_s, k_b) = \frac{c^2}{4\pi\epsilon_0}\left(k_b^2(\hat{\mathbf{x}}_s \times \mathbf{p}) \times \hat{\mathbf{x}}_s + (3\hat{\mathbf{x}}_s(\hat{\mathbf{x}}_s \cdot \mathbf{p}) - \mathbf{p}) \right.$$
$$\left. \times \left(\frac{1}{x_s^2} - i\frac{k_b}{x_s}\right)\right)\frac{e^{ik_b x_s}}{x_s}, \quad (2)$$

where $\hat{\mathbf{x}}_s$ is the unit vector and $x_s = ||\mathbf{x}_s||^2$ is the Euclidean distance. The dipole source $\mathbf{p}$ is described by a gamma distribution (Shakas

& Linde 2015) to allow for variations in the radiated electric field, $\mathbf{E}_s$. The 3-D Cartesian vectors $\mathbf{x}_s$ and $\mathbf{x}_r$ point from the source to the thin-bed centre and from the thin-bed centre to the receiver, respectively (see Fig. 1). The thin-bed reflection coefficients, $\mathbf{R}_e$, are given by (Orfanidis 2002, section 7.2):

$$\mathbf{R}_e(k_b, k_a, \theta) = \frac{\mathbf{R}(1 - e^{-2iak_a\cos\theta})}{1 - \mathbf{R}^2 e^{-2iak_a\cos\theta}}, \quad (3)$$

where $\mathbf{R}$ may represent the TE or TM Fresnel reflection coefficient and the incidence angle θ is determined by the orientation of the vectors $\mathbf{x}_s$ and $\mathbf{x}_r$. Eq. (3) is not restricted to modelling a thin-layer but also reduces to the Fresnel reflection coefficients as the aperture increases (Lai *et al.* 2002), making the exponential term negligible.

Uncertainties in the forward modelling process, such as the coupling of the source and/or receiver, are often treated separately (e.g. Grégoire & Hollender 2004; Deparis & Garambois 2008). Here, we use $\mathbf{F}(*)$ to indicate source and receiver related modelling uncertainties, making our forward model analogous to the ones used by other authors. For the modelling exercises to follow, we set $\mathbf{F}(*) = 1$, since we use the same (known) source for both the effective-dipole and thin-bed forward models. Finally, the last term on the right hand side of eq. (1) accounts for the dispersion, attenuation and spherical spreading of the reflected electric field propagating from the thin-bed to the receiver.

2.2 GPR response from a homogeneous fracture

In order to make a valid comparison between the thin-bed and effective-dipole forward responses, we must define an appropriate modelling domain such that the fracture is large enough to avoid that its edges contribute significantly to the reflected response. To accomplish this, we consider a square fracture with side length L and centre $\mathbf{C}$ that is separated from both source and receiver by S. The source-receiver offset is given by D and the normal to the fracture plane at $\mathbf{C}$ runs through the source-receiver midpoint. A schematic of this model is shown in Fig. 1.

The fracture side length L must be large compared to the maximum source-receiver offset so that the boundaries do not affect the actual GPR response. The minimum side length necessary is expected to be inversely related to the maximum source-receiver offset ($D_{\max}$). To compute this length, we set $D_{\max} = 2$ m and create fractures with side length $L = \{5, 8, 10, 20, 30, 40, 50, 60\}$ m. We then simulate the GPR reflection data from these fractures, using the effective-dipole method, for different fracture apertures and conductivities $a = \{0.1, 1, 10\}$ mm and $\sigma = \{0.01, 0.1, 1\}$ S m^{-1}, respectively, and a constant relative electric permittivity, $\epsilon_r = 81$. In Fig. 2, we present the simulated reflected traces for $L = \{5, 8, 10\}$ m, $a = 1$ mm and $\sigma = 0.1$ S m^{-1}. The effect of the fracture boundaries (also verified with FDTD simulations that are not shown here) manifests as a secondary reflection that diminishes and arrives later with increasing L (e.g. Pearce & Mittleman 2002). For $L \geq 20$ m, we find that the difference in simulated amplitudes to the $L = 60$ m response is less than 0.01 per cent. This is very small compared with typical error levels and we set $L = 20$ m in the following simulations.

2.3 Fractures with heterogeneous properties

Natural fractures barely resemble thin-beds. Rock fractures are often the result of normal and shear stresses that create void space between two rough surfaces (National Research Council, Committee
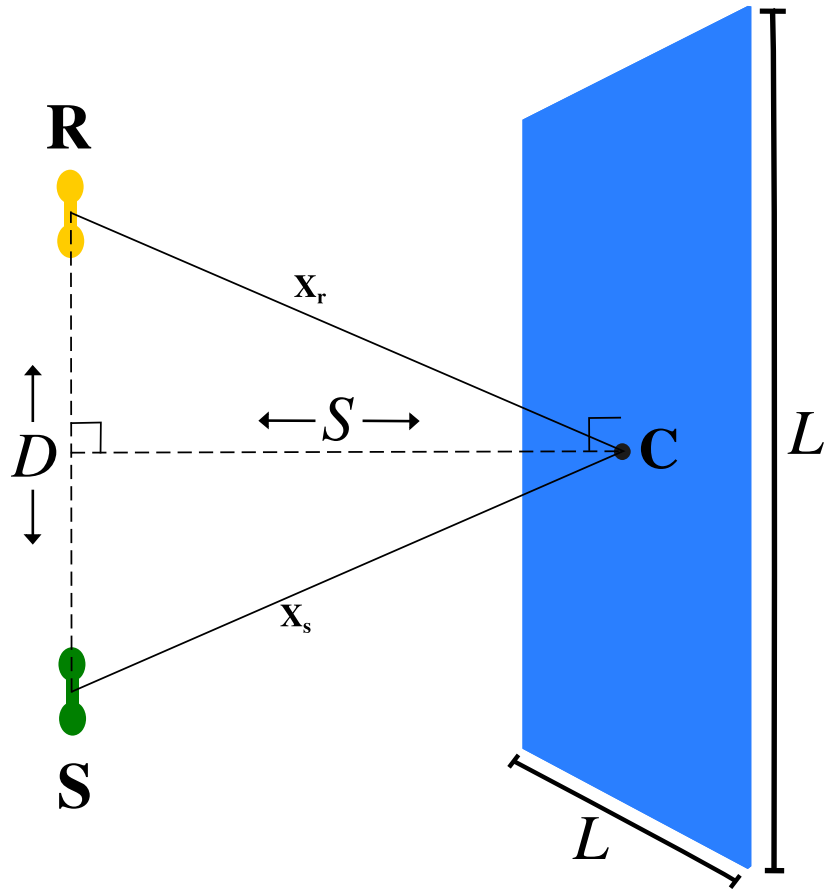
Figure 1. Schematic of the fracture model and the acquisition geometry. The source (**S**) and receiver (**R**), offset by a distance D, are separated by the fracture by a distance S. The fracture midpoint is **C** and has a side length L. For the thin-bed forward model, the source propagates to the fracture midpoint and back to the receiver, shown by the vectors $\mathbf{x}_s$ and $\mathbf{x}_r$ respectively.
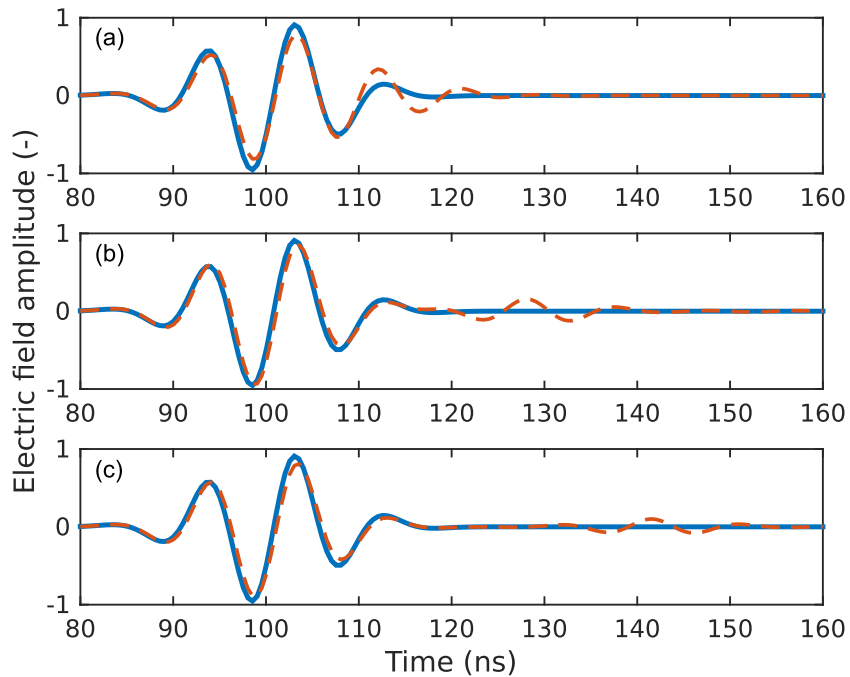

Figure 2. Simulated reflected traces for fractures with $a = 5$ mm and L equal to (a) 5 m, (b) 8 m and (c) 10 m. Acquisition parameters are $S = 5$ m and $D = 2$ m (see Fig. 1). Results are presented for the thin-bed (solid) and effective-dipole (dashed) forward models. For each model type, the response is normalized such that the maximum amplitude is 1.

on Fracture Characterization and Fluid Flow 1996). The point-wise separation between the two surfaces is termed local aperture (Oron & Berkowitz 1998).

For the effective-dipole method, we assume that a fracture is composed of a collection of parallel plates. Each parallel plate has a unique aperture a and represents one dipole element on which the thin-bed reflection coefficients, eq. (3), apply locally. Since eq. (3) is also valid for apertures above the thin-bed criterion, it can be used to model reflections from a fracture with apertures both above and below $\frac{3\lambda}{4}$. Furthermore, changes in the polarity of the incoming electric field (e.g. due to the varying separation from the source or due to the antenna radiation pattern) imply that reflections from apertures above and below $\frac{3\lambda}{4}$ may interfere both constructively and destructively. In practice, however, the fracture aperture is almost always well below the thin-bed criterion (typically by one or two orders of magnitude).

2.3.1 Self-affine aperture distributions

Local aperture variations are typically strong (e.g. Adler & Thovert 1999, Ch. 4) and often exhibit statistically similar patterns over several scales (Bonnet *et al.* 2001). Such patterns can be reproduced mathematically by self-affine functions (Mandelbrot 1982). Here, we represent heterogeneity in local aperture using the power spectrum approach by Adler & Thovert (1999) to create self-affine surfaces (see their section 2.3.2 for details). The technique is based on taking the Fourier transform of a 2-D Gaussian random field and generating a correlated random field using the following autocorrelation function:

$$C_h(u) = \sigma_h^2 \exp\left[-\left(\frac{u}{l_c}\right)^{2H} \right], \tag{4}$$

with input parameters being the variance σ_h, the cut-off length l_c and the Hurst exponent H. The cut-off length is the characteristic length over which correlations disappear and the Hurst exponent, that varies over the range $0 \leq H \leq 1$, is related to the fractal dimension (FD) through $FD = 3 - H$ (Shepard *et al.* 1995).

2.3.2 Dipole coupling

Our effective-dipole forward model (Shakas & Linde 2015) is based on an analogy to the microscopic analysis of Maxwell's equations (e.g. Purcell 2011, Ch. 10). From a microscopic viewpoint, the polarization of dielectrics is a result of the cumulative contribution of many discrete polarizable elements. These elements are primarily polarized by the incoming electromagnetic field from an external source. In Shakas & Linde (2015), we upscaled the microscopic treatment to model propagation and scattering of GPR from fractures. We accomplished this by discretizing a fracture into dipole elements, where each element acts as a secondary source that is polarized by the GPR source (see Fig. 3).

Apart from energy from the source, each dipole element also receives energy from all the other elements (dipole coupling). When a fracture is planar (no topography), all dipole elements have the same orientation. This implies that the electric field always propagates perpendicularly between elements of the same fracture. A close look at eq. (3) reveals that when $\theta = \frac{\pi}{2}$ (i.e. perpendicular propagation), the exponential term reduces to unity and the thin-bed reflection coefficient reduces to zero. Therefore, for a planar fracture there is no contribution from dipole coupling. When fracture topography and/or multiple fractures are present, dipole cou-

pling must be taken into account and this increases the computation time of our effective-dipole method. In this study, we consider only individual and planar fractures.

2.3.3 GPR response of a fracture with a heterogeneous conductivity distribution

In hydrogeophysical applications, GPR has been used to monitor electrically conductive tracer tests in fractured rock (e.g. Lane *et al.* 2000; Tsoflias *et al.* 2001; Talley *et al.* 2005; Tsoflias & Becker 2008; Dorn *et al.* 2011; Shakas *et al.* 2016). Due to the non-linear nature of flow and transport in fractures, the resulting tracer distribution will be highly heterogeneous. On this basis, we create a test-case to ensure that the simulations based on our effective-dipole method are in agreement with FDTD simulations (gprMax3D, Warren *et al.* 2015).

In a realistic fracture, the aperture variation would directly (by an increase in the overall conductance) and indirectly (by governing the transport of the electrically conductive tracer) affect the GPR response. However, in order to adequately capture the effect of aperture variations, the discretization in FDTD simulations must be several times smaller than the smallest fracture aperture. This makes it difficult to accurately model aperture variations with FDTD and instead, we choose to keep the aperture constant and only vary the electrical conductivity.

We define a 10 m × 10 m × 10 m modelling domain with a discretization step of 1 cm. Within this domain, we define an 8 m × 8 m square fracture with an aperture of 10 cm, to allow for FDTD simulations with at least 10 nodes within the fracture. Along the fracture plane we assign the electrical conductivity distribution using the autocorrelation function in eq. (4) with $\sigma_h = 0.025$, $l_c = 1$ and $H = 0.5$. The mean conductivity is $\sigma = 0.05$ S m^{-1} (schematic in Fig. 4a and the relative electric permittivity $\epsilon_r = 21$, which results in a dominant wavelength of 65 cm within the fracture, thus making the fracture a thin-bed. As a source, we use a Ricker wavelet centred at 100 MHz that is emitted by a vertically oriented infinitesimal dipole. To obtain a comparable source wavelet to the one in gprMax3D, we model the propagation to the first receiver (from S to R1) and run a local optimization search to find the best fitting source parameters.

We present the effective-dipole and gprMax3D simulation results in Fig. 4(b). Note that gprMax3D works in the time-domain and the effective-dipole method in the frequency domain. Therefore, Inverse Fourier-transformed traces are shown in the latter case. The excellent agreement between the two different approaches confirms that the heterogeneous fracture is modelled well with the effective-dipole method and it confirms that dipole coupling does not contribute to the response for planar and individual fractures.

3 ESTIMATION OF FRACTURE APERTURE

Except for an unknown fracture aperture, we consider an idealized case for which all other fracture parameters are known, namely, the exact form of the source wavelet, the electric properties of both the rock matrix and the fracture filling as well as the orientation and position of the fracture. In this case it is straightforward to estimate an effective apparent aperture using GPR measurements for at least two source-receiver offsets.
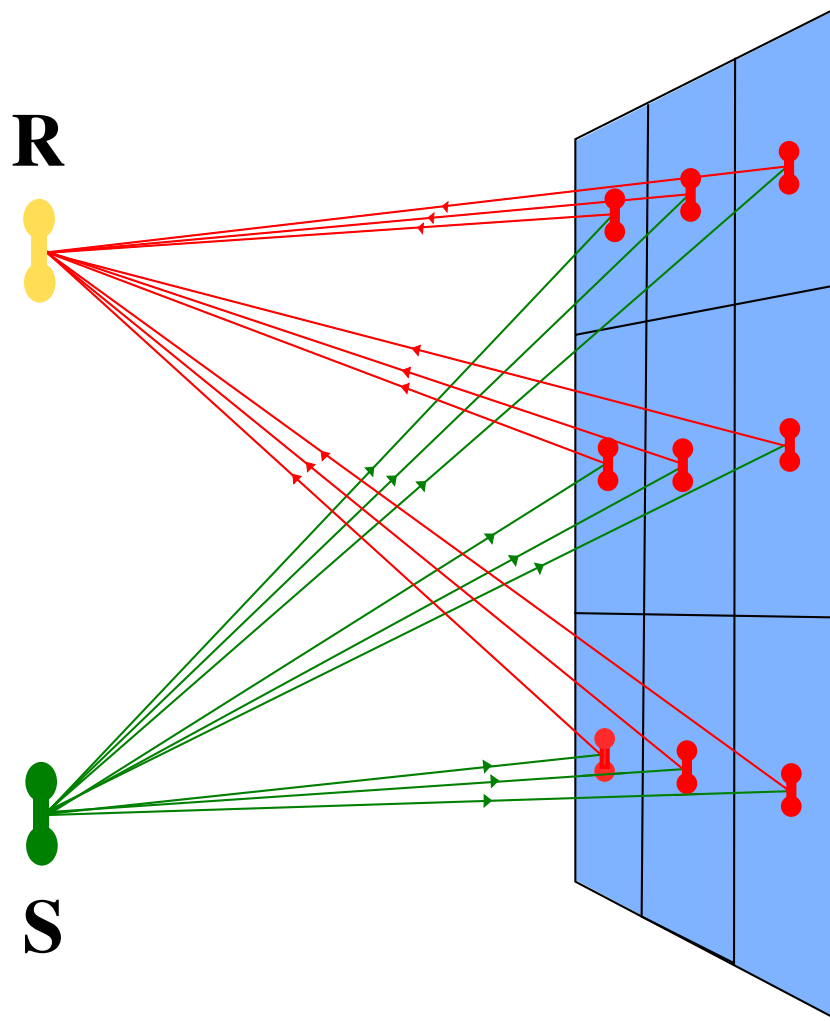
Figure 3. Schematic of the effective-dipole forward modelling framework. A fracture is discretized into elements, and each element receives energy (green) directly from the source (S) and radiates (red) back to the receiver (R).

3.1 Synthetic data creation

In both the homogeneous and heterogeneous fracture simulations that follow, the synthetic GPR data are created using the effective-dipole method. Since both the effective-dipole and thin-bed forward models are formulated in the frequency domain, we choose to treat the data, for inversion purposes, also in the frequency domain. For each fracture realization, the data consists of two traces that correspond to source-receiver offsets of $D = 0$ m and $D = 2$ m and with a constant separation between the fracture and antennas set to $S = 5$ m. The same vertically oriented source is used in all simulations. The source spectrum consists of a Ricker wavelet that is peaked at 100 MHz and we compute the reflected response in the range of $0 < f_n \leq 300$ MHz at a sampling rate of 1 MHz. Each resulting trace consists of 300 complex-valued numbers representing the returning electric field.

3.2 Amplitude scaling and noise-contamination

The thin-bed forward model computes the source-fracture-receiver interaction for a single path of the electromagnetic field, while the effective-dipole forward model computes it as an integral of many interactions on the finite fracture plane (compare Figs 1 and 3).

This leads to an amplitude discrepancy between the returning electric fields that are computed from the two methods. In practice, this limitation of the thin-bed approach can be avoided by taking GPR measurements with varying source-receiver offsets and considering the amplitude and phase variations as a function of offset. Therefore, with a minimum of two offsets we can compute relative amplitude-phase variations. In all the computations that follow, we compute the largest (absolute value) amplitude of the $D = 0$ reflection, $\max(|E_z(\omega)|)$, and use it to scale the response for each offset and each frequency component individually. This gives, for both the thin-bed and effective-dipole forward models, responses for which the $D = 2$ m response is scaled relative to the $D = 0$ m response. We then contaminate each frequency component using Gaussian noise with standard deviation of 0.035 (3.5 per cent) that we add separately to the real and imaginary parts. This amounts to 5 per cent noise in the time-domain data and is representative of the noise level in high-quality field data (e.g. Shakas *et al.* 2016, fixed antenna experiment).

3.3 Data inversion

In deterministic geophysical inversion of GPR data, the aim is often to minimize a data misfit function in order to derive the
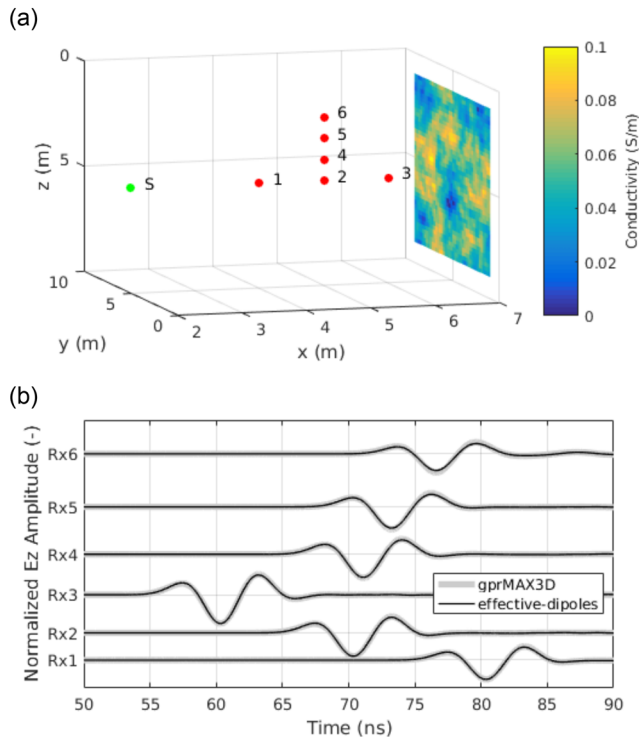
Figure 4. (a) The model used to compare the effective-dipole modelling results with those obtained from 3-D FDTD modelling for the case of a heterogeneous conductivity distribution. The source (S) is placed 5 m away from an 8 m × 8 m fracture with strong conductivity variations. The six receiver locations are also shown. (b) The simulation results from the model in (a) based on 3-D FDTD (gprMax) and the effective-dipole method agree very well.

best-fitting fracture parameters that reproduce the observed data using the forward model (e.g. Grégoire & Hollender 2004; Bradford & Deeds 2006; Deparis & Garambois 2008; Sassen & Everett 2009). The test case we are considering (i.e. all parameters known except the aperture) is idealized and serves as a best-case scenario. This implies that any problems that appear in this setting will certainly be present in actual field situations.

The misfit function space can be complex, especially when the forward model is nonlinear. In order to invert the noise-contaminated data for the best-fitting aperture, we use the golden search algorithm (Kiefer 1953) with the weighted root mean square error (WRMSE) as misfit function:

$$WRMSE\left(d_i^{\text{sim}}, d_i^{\text{obs}}, \text{sd}\right)$$

$$= \sqrt{\frac{1}{2N}\sum_i^N \frac{\Re\{d_i^{\text{sim}} - d_i^{\text{obs}}\}^2 + \Im\{d_i^{\text{sim}} - d_i^{\text{obs}}\}^2}{\text{sd}^2}} \quad (5)$$

where d_i^{sim} is the simulated data and d_i^{obs} is the observed data with added independent and identically distributed (iid) Gaussian noise of standard deviation sd. The WRMSE is 1 when the average misfit between simulated and observed data corresponds to the predefined noise level. Our convergence criteria for the inversion are that (1) the WRMSE ≤ 1 or (2) the forward model is run more than 1500 times.

3.4 Fractures with a constant aperture

We use the golden search algorithm to find the best-fitting aperture given noise-contaminated data generated from the GPR response

of a homogeneous fracture. Using the effective-dipole code, we create 40 data sets for fractures with constant aperture that varies logarithmically in the range 0.1 mm ≤ a ≤ 10 mm. Then, using both the thin-bed and effective-dipole forward models we run the inversion algorithm until one of the two criteria is met. In Fig. 5, we show the best-fit aperture along with the WRMSE for both forward models. Considering three different fracture conductivities, we find that inversion results based on the thin-bed or effective-dipole forward models produce excellent aperture estimates, down to apertures of 0.3 mm.

3.5 Fractures with heterogeneous aperture variations

In nature, fractures exhibit variations in local aperture that will cause GPR reflections to differ from the theoretical thin-bed reflection of a homogeneous fracture. These apertures are often assumed to follow specific spatial patterns along the fracture plane. Here, we assess the impact of local aperture heterogeneity on the inferred thin-bed aperture.

Using the geostatistical algorithm by Adler & Thovert (1999), presented in Section 2.3.1, we consider 16 classes of heterogeneity models describing local aperture. Each class is defined by a unique pair of the cut-off length and Hurst exponent, namely $H = \{0.25, 0.5, 0.75, 1\}$ and $l_c = \{0.5, 1, 2, 4\}$ m, and for each class we generate 1000 fracture realizations. We discretize the heterogeneous fractures using 10 elements per dominant wavelength, resulting in a spatial element discretization of 10 cm × 10 cm. All fractures share the same (arithmetic) mean aperture of 5 mm, variance of 1 mm and electrical conductivity $\sigma = 0.1$ S m^{-1}. One representative realization for each geostatistical class is shown in Fig. 6.

For each fracture realization we use the effective-dipole forward model to create noise-contaminated GPR (observed) data. Using the thin-bed forward model and the golden search inversion algorithm, we infer the best-fitting constant-aperture fracture that can reproduce the observed data. The histograms of the inferred apertures for each $\{H, l_c\}$ pair are plotted in Fig. 7 together with the marginal probability density function (pdf) of aperture for the geostatistical models considered. The corresponding mean and variance of the WRMSE, for each geostatistical class, are shown in Table 1. For comparison purposes, we also tabulate the mean and variance of the WRMSE between the observed data and simulated data from a fracture with constant aperture of 5 mm (equivalent to the mean aperture of the 16 classes of geostatistical models).

3.6 GPR resolution and weighted apertures

Considering the same source-receiver and fracture geometry as in Fig. 3, we can define (1) the radial resolution as the smallest aperture and (2) the lateral resolution as the smallest feature along the fracture plane that can be reliably inferred by the GPR data (e.g. Jol 2008, section 1.3.4).

In a water-saturated fractured rock system it is possible to obtain very high radial resolution because of the strong contrast between electrical parameters in the rock matrix and fracture filling. For example, our inversion results for the homogeneous fracture (Fig. 5) suggest that we can reliably infer apertures down to roughly 0.3 mm with a signal whose dominant wavelength is 1 m.

Lateral resolution of GPR data is often discussed in terms of the Fresnel zone (Pearce & Mittleman 2002) and it is used to approximate the smallest detectable target for a given acquisition geometry and signal bandwidth. The Fresnel zone is derived by
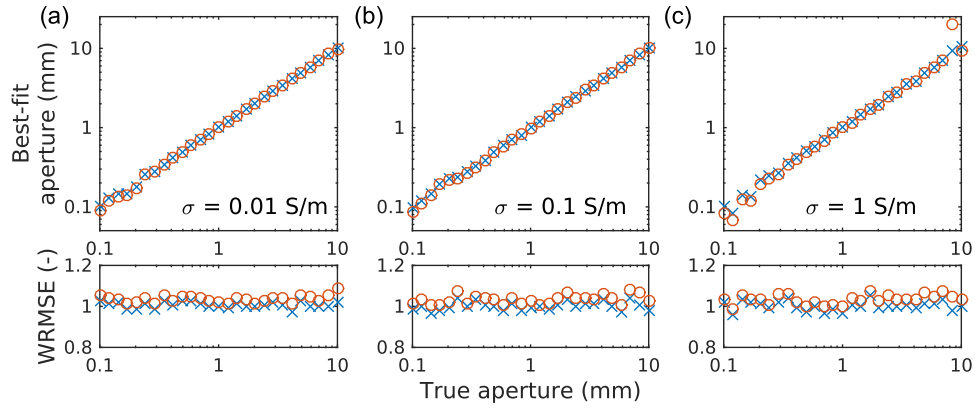
Figure 5. Inversion results, along with corresponding WRMSE, for the best-fit aperture describing a homogeneous fracture. The inversions use noise-contaminated (observed) data generated using the effective-dipole model, and (simulated) forward responses from either the thin-bed ($\circ$) or the effective-dipole ($\times$) models. Three fracture conductivities (σ) are considered for 40 fracture apertures in the logarithmically spaced interval $0.1 \leq a \leq 10$ mm.
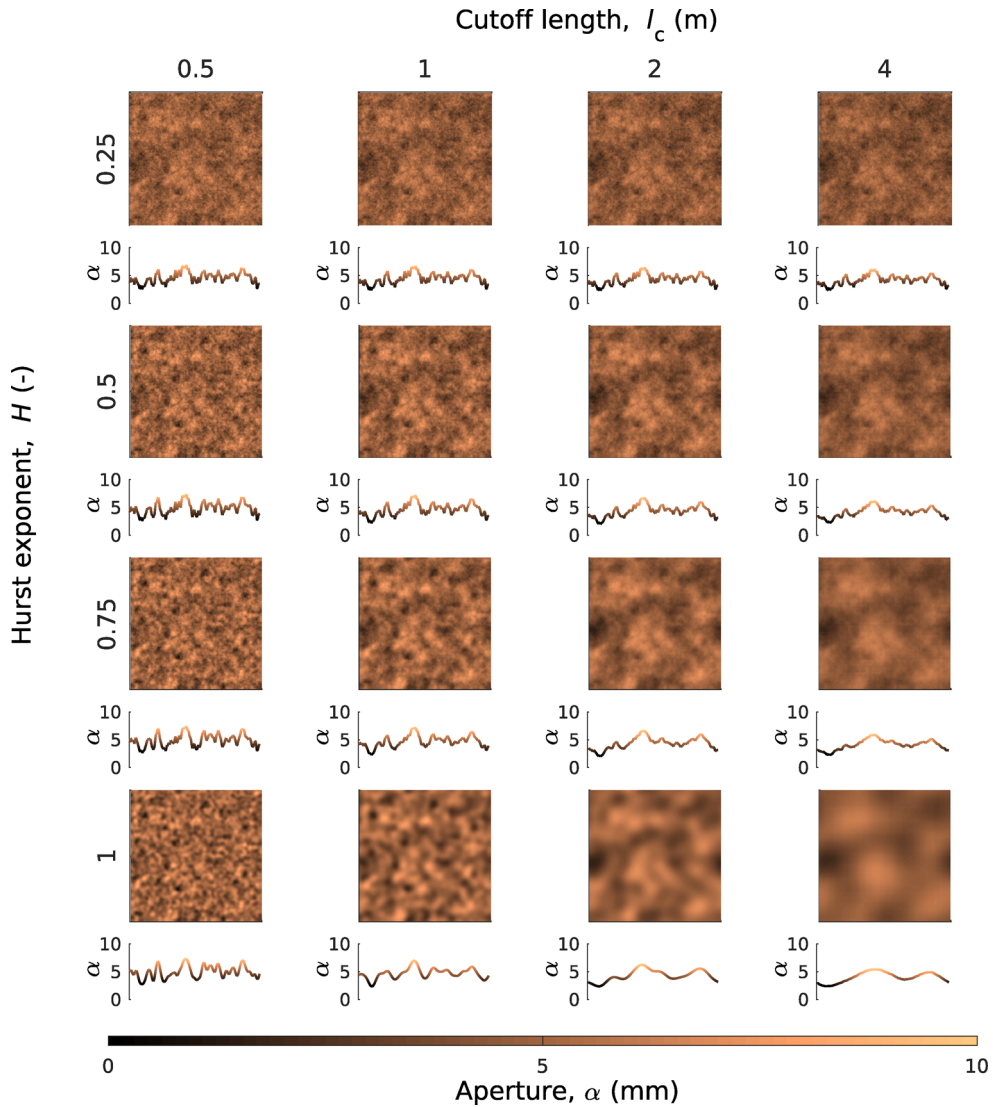

Figure 6. Representative aperture (α) realizations for each of the 16 considered geostatistical heterogeneity classes. Each class is characterized by a different pair of Hurst exponent (H) and cut-off length (l_c). The mean aperture is 5 mm, the variance is 1 mm and the fracture size is 20 m $\times$ 20 m. Below each realization, the aperture profile along the horizontal line dissecting the middle of each fracture is shown.
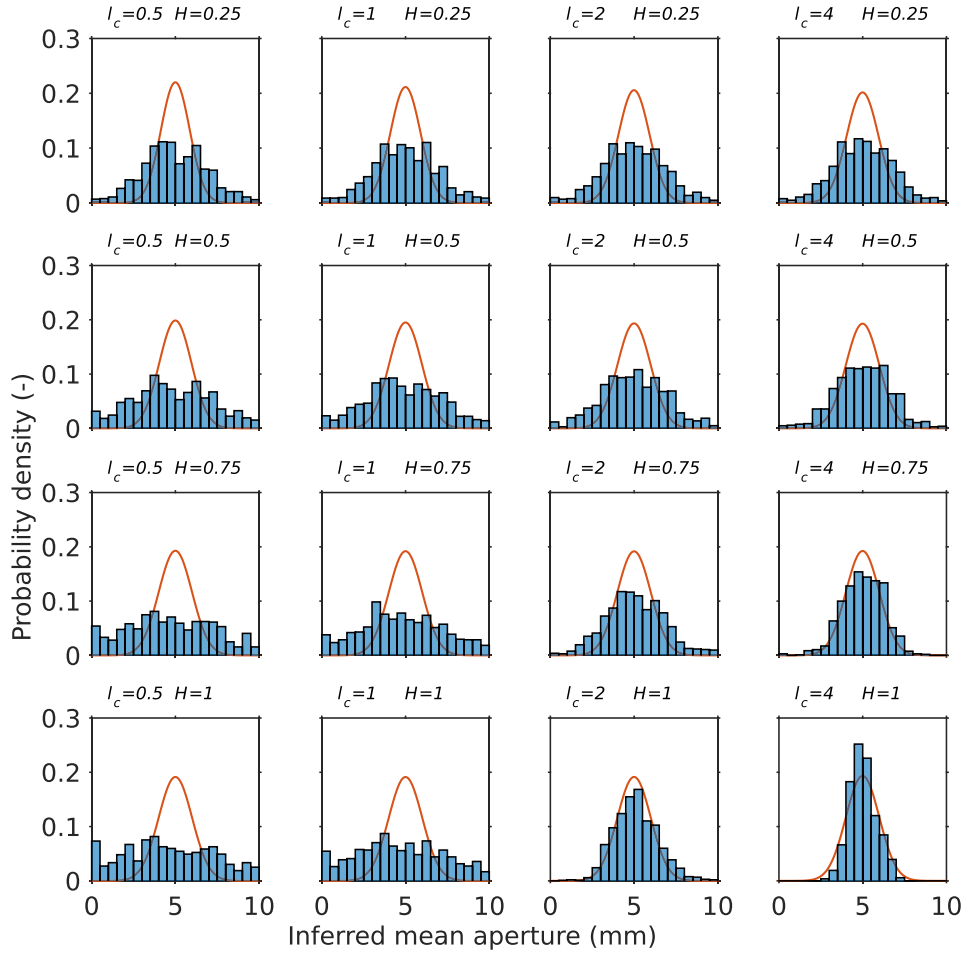
Figure 7. Probability density histograms of the best-fitting homogeneous fracture apertures (1000 realizations for each class). For each class of heterogeneity model, the marginal probability density function of aperture is the same (solid red line). The corresponding mean and standard deviation of the WRMSE, for each class, is shown in Table 1.

Table 1. {Mean, variance} of the WRMSE between simulated data, computed using the thin-bed forward model and assuming a homogeneous fracture with either (A) the best-fitting inferred aperture (see Fig. 7) or (B) a 5 mm aperture, and observed data computed using the effective-dipole forward model and considering a fracture with a heterogeneous aperture field (with arithmetic mean of 5 mm). In total, 16 classes of heterogeneity are generated by varying the Hurst exponent H and cut-off length l_c.

	$l_c = 0.5$ m	$l_c = 1$ m	$l_c = 2$ m	$l_c = 4$ m
(A) Homogeneous fracture with best-fitting aperture				
$H = 0.25$	{1.103, 0.005}	{1.093, 0.004}	{1.080, 0.003}	{1.067, 0.003}
$H = 0.5$	{1.157, 0.010}	{1.109, 0.006}	{1.069, 0.003}	{1.045, 0.002}
$H = 0.75$	{1.189, 0.016}	{1.090, 0.005}	{1.043, 0.002}	{1.025, 0.001}
$H = 1$	{1.210, 0.024}	{1.064, 0.004}	{1.025, 0.001}	{1.016, 0.001}
(B) Homogeneous fracture with 5 mm aperture				
$H = 0.25$	{1.923, 0.123}	{1.917, 0.120}	{1.905, 0.108}	{1.893, 0.095}
$H = 0.5$	{1.981, 0.227}	{1.949, 0.210}	{1.912, 0.139}	{1.883, 0.084}
$H = 0.75$	{2.013, 0.285}	{1.958, 0.296}	{1.899, 0.120}	{1.865, 0.047}
$H = 1$	{2.033, 0.313}	{1.957, 0.370}	{1.889, 0.076}	{1.856, 0.018}

considering a wave with normal incidence to a reflecting surface. Moving away from this point of incidence, the first Fresnel zone radius is constructed by computing the separation at which another incident wave (from the same source) is reflected with a phase shift $\Delta\phi \leq \pi$. For the acquisition geometry we consider here, and a

signal with dominant wavelength of 1 m in the background matrix, the resulting Fresnel zone radius is 1.6 m. However, this does not provide information about the relative contribution to the measured signal within this radius.

Instead of using the Fresnel zone, we describe here the lateral resolution by considering the individual response of each discretized element for a homogeneous fracture. Using the same source and acquisition geometry as above, we generate a fracture discretized by 10 cm × 10 cm elements with $\sigma = 0.1$ S m^{-1} and $a = 5$ mm. We then compute, for each of the two source–receiver pairs, the returning (vertical) electric field from each element. This amounts to a complex-valued contribution, for each sampled frequency, that represents the amplitude and phase of the electric field from each element. Next, we sum the complex-valued response over all frequencies. We do this for each element and source–receiver offset separately. This provides two complex-valued numbers for each element (one for each source–receiver offset). We then take the absolute value of the pair above and sum the two values. The result is a real-valued number per element that provides us a distribution of weights along the fracture plane. Finally, we scale the weight distribution such that it integrates to 1. The final weights are shown in Fig. 8 along with the first Fresnel zone.

These weights allow us to compute a mean aperture for each fracture realization over a spatial scale that corresponds well to the first Fresnel zone. As an example, in Fig. 9 we show the application of
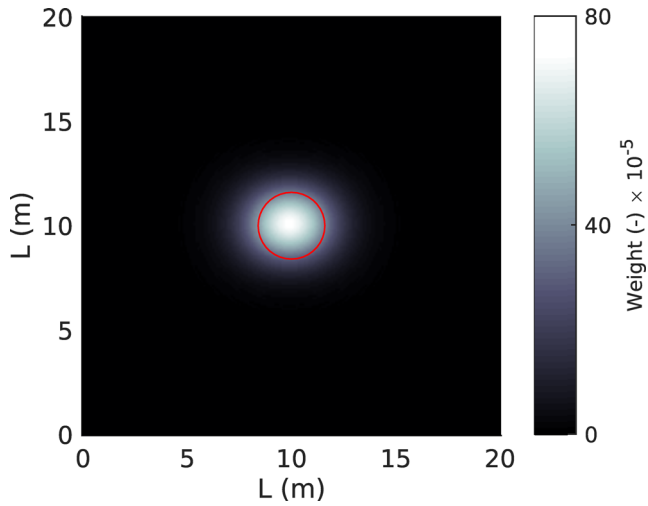
Figure 8. Weights derived from the sensitivity of the effective-dipole forward model, for a homogeneous fracture. Fracture aperture is $a = 5$ mm and conductivity is $\sigma = 0.1$ S m^{-1}, respectively. Acquisition parameters are $S = 5$ m, $D = 0$ m and $D = 2$ m and $L = 20$ m (see Fig. 1). The first Fresnel zone is indicated by a red solid line.

the weights to the fracture realization presented in Fig. 6. However, this averaging is built on the assumption that the apertures influence the GPR data linearly and does not always correspond to the best-fitting inferred aperture. In Fig. 10, we show, for each $\{H, l_c\}$ combination, a scatter plot of the inferred versus weighted aperture pairs. In most cases, the agreement is very poor.

4 DISCUSSION

The thin-bed forward model can serve as a reliable simulator of the GPR response from a homogeneous fracture that is large enough to be considered 'infinite'. The inversion results (Fig. 5) suggest that the thin-bed and effective-dipole forward models work equally well in retrieving the (constant) aperture. Reliable estimates are obtained over a wide aperture range, down to apertures that are more than three orders of magnitude smaller than the dominant wavelength of the GPR source.

Natural fractures result from complex processes and are (most probably) never homogeneous. The primary objective of this study was to understand the influence of small-scale aperture heterogeneity on the inferred thin-bed aperture. We accomplish this by defining 16 classes of geostatistical models, and creating 1000 fracture
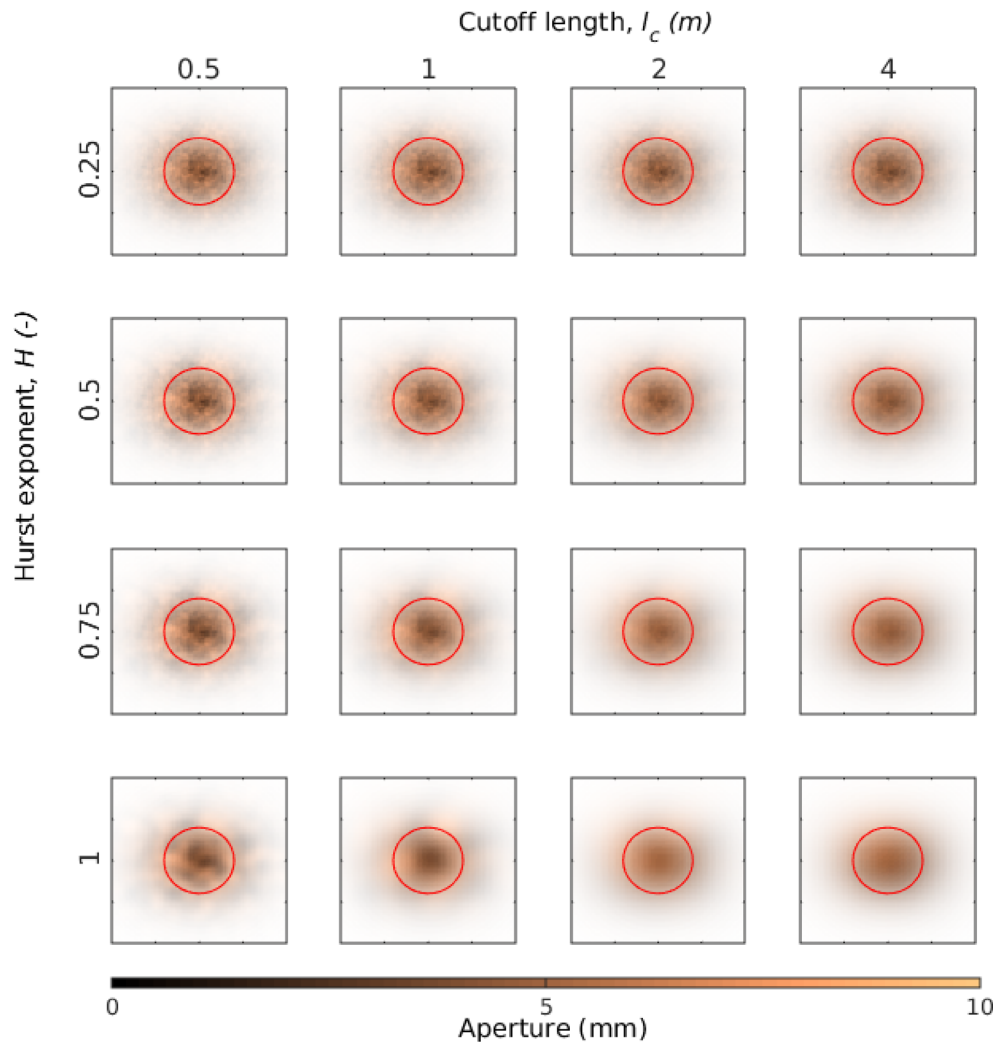

Figure 9. The averaging process implied by the linear weights in Fig. 8 is illustrated for the same fracture realizations as in Fig. 6. The opacity is complete for elements with negligible weight and the opacity is decreased linearly to zero for the elements with the highest sensitivity. The first Fresnel zone is shown by a red solid line. For better visualization, only the central 8 m × 8 m section of the full 20 m × 20 m fractures is shown.
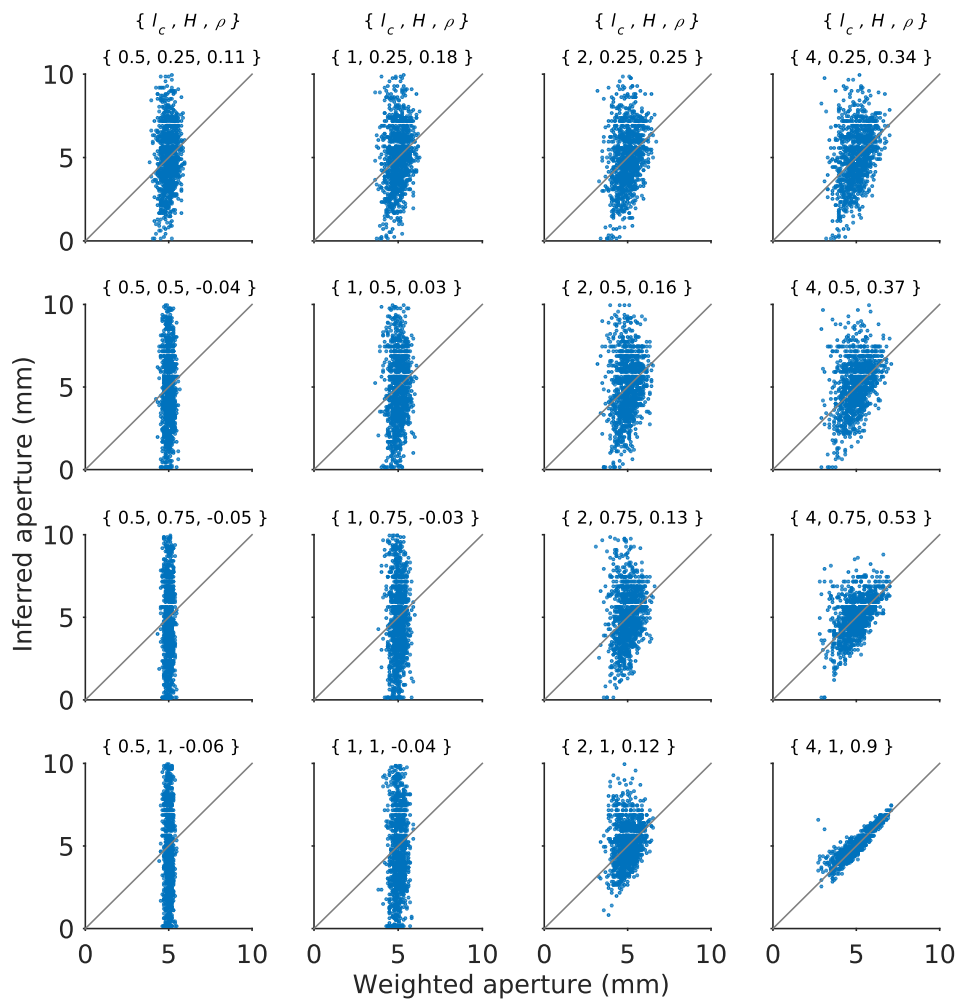
Figure 10. For each of the 16 classes of geostatistical models, scatter plots of the inferred (apparent) versus the weighted (mean) aperture for 1000 fracture realizations. The linear trend is plotted with a diagonal line and the Hurst exponent H, cut-off length l_c and correlation coefficient ρ is given for each plot.

realizations within each class. We then use our effective-dipole forward model to create noise-contaminated data sets, and use the thin-bed forward model to infer a corresponding homogeneous fracture that best fits each data set. If the GPR response would only be a linear average of the actual apertures over the Fresnel zone, then the inferred apertures should show significantly less variability than the marginal pdf of the geostatistical models. Our results suggest that this is not the case (see Fig. 7) and only when the cut-off length l_c is large (i.e. as aperture patterns become larger) does the histogram of inferred apertures approach the marginal pdf of the actual local apertures. This convergence is intuitive because as the size of patterns increase, the realizations approach the case of a homogeneous-aperture fracture. Furthermore, the Hurst exponent H also plays an important role. Small H suggests more fractal behaviour, resulting in similar aperture patterns appearing at all spatial scales. The inferred aperture distributions for small H (first row in Fig. 7) show a very similar pattern, regardless of changes in l_c.

The fact that the inferred apertures are much wider than the marginal pdf of the actual (geometric) apertures for cases when l_c and/or H are small, suggests that the inferred GPR aperture is not a good proxy of the geometric aperture. In fact, the inferred GPR aperture should be considered as an apparent aperture. The situation is similar in other branches of geophysics. For example, in electrical resistivity tomography it is possible to obtain negative apparent re-

sistivities, even if electrical resistivity can never be negative. These effects are manifestations of nonlinearity and imply that apparent properties might be difficult to translate into actual properties. Table 1 also highlights that the derived apparent apertures explain the data well (WRMSE slightly higher than 1) while simulations based on the constant aperture of 5 mm fit the data poorly (WRMSE around 2).

To better understand to what extent the data can be seen as a linear spatial averaging process, we derive weights based on the complex-valued returning electric field from each fracture element (local aperture). This is done for a fracture with a constant aperture that equals the mean aperture of the geostatistical models. The resulting weights (see Fig. 8) are significant within the first Fresnel zone. We use these weights to compute a weighted aperture for each fracture realization (Fig. 9). In contrast, the apparent aperture is obtained from the homogeneous fracture that can best reproduce the data through the thin-bed forward model. The comparison between the derived weighted aperture and the apparent aperture (Fig. 10) suggests that when the cut-off length is small, the apparent aperture does not correspond well to the weighted aperture (first column). While the apparent aperture prediction approaches the linear estimate as the cut-off length is increased, good correspondence of the two apertures is only obtained when both l_c and H are large, as in the pair $\{H, l_c\} = \{1, 4\,\text{m}\}$.

5 CONCLUSIONS

For an idealized experimental set-up, we have used the GPR thin-bed forward model to infer an apparent fracture aperture. When data are generated from a homogeneous (constant-aperture) fracture model, the apparent aperture corresponds well with the actual fracture aperture, However, when aperture heterogeneities are present, the apparent aperture that is derived under the assumption of a homogeneous fracture does not always provide satisfying results. Namely, when a small cut-off length (aperture heterogeneity patterns are small) and Hurst exponent (heterogeneity present at all scales) is used to generate aperture fields, the apparent aperture can be very different from the mean aperture averaged over the first Fresnel zone. When aperture variations are non-fractal ($H = 1$) and the aperture patterns are large ($l_c = 4$ m) compared to the signal dominant wavelength (1 m), the apparent aperture can be a good estimate of the Fresnel-based linear average of fracture aperture.

Our results suggest that GPR-derived estimates of fracture aperture, that are based on the common assumption of constant aperture, should be treated with caution, especially when strong aperture heterogeneity is present. Under the homogeneous assumption, inferred apertures serve as an apparent estimate that has a complex and nonlinear relation to the actual geometrical fracture aperture. To reliably interpret GPR data generated by a heterogeneous fracture, a more encompassing modelling framework must be considered, that explicitly accounts for aperture heterogeneity. In future work, we plan to use model selection tools to determine the geostatistical model that best corresponds to GPR reflection data from heterogeneous fractures.

ACKNOWLEDGEMENTS

REFERENCES

Adler, P.M. & Thovert, J.F., 1999. *Fractures and Fracture Networks,* Kluwer Academic Publishers, vol. 15, p. 429.

Babcock, E. & Bradford, J.H., 2015. Reflection waveform inversion of ground penetrating radar data for characterizing thin and ultrathin layers of nonaqueous phase liquid contaminants in stratified media, *Geophysics,* **80**(2), H1–H11.

Bonnet, E., Bour, O., Odling, N.E., Davy, P., Main, I., Cowie, P. & Berkowitz, B., 2001. Scaling of fracture systems in geological media, *Rev. Geophys.,* **39**(3), 347–383.

Bradford, J.H. & Deeds, J.C., 2006. Ground penetrating radar theory and application of thin-bed offset-dependent reflectivity, *Geophysics,* **71**(1), K47–K57.

Day-Lewis, F.D., Lane, J.W., Harris, J.M. & Gorelick, S.M., 2003. Time-lapse imaging of saline-tracer transport in fractured rock using difference-attenuation radar tomography, *Water Resour. Res.,* **39**(10), doi:10.1029/2002WR001722.

Deparis, J. & Garambois, S., 2008. On the use of dispersive APVO GPR curves for thin-bed properties estimation: theory and application to fracture characterization, *Geophysics,* **74**(1), J1–J12.

Dorn, C., Linde, N., Le Borgne, T., Bour, O. & Baron, L., 2011. Single-hole GPR reflection imaging of solute transport in a granitic aquifer, *Geophys. Res. Lett.,* **38**, L08401, doi:10.1029/2011GL047152.

Dorn, C., Linde, N., Doetsch, J., Le Borgne, T. & Bour, O., 2012. Fracture imaging within a granitic rock aquifer using multiple-offset single-hole and cross-hole GPR reflection data, *J. appl. Geophys.,* **78**, 123–132.

Fearn, H., James, D.F. & Milonni, P.W., 1996. Microscopic approach to reflection, transmission, and the Ewald-Oseen extinction theorem, *Am. J. Phys.,* **64**(8), 986–994.

Grasmueck, M., 1996. 3-D ground-penetrating radar applied to fracture imaging in gneiss.*Geophysics,* **61**(4), 1050–1064.

Grégoire, C. & Hollender, F., 2004. Discontinuity characterization by the inversion of the spectral content of ground penetrating radar (GPR) reflections-Application of the Jonscher model, *Geophysics,* **69**(6), 1414–1424.

Grobbe, N. & Slob, E.C., 2016. Seismo-electromagnetic thin-bed responses: Natural signal enhancements?, *J. geophys. Res.,* **121**(4), 2460–2479.

Jeannin, M., Garambois, S., Grégoire, C. & Jongmans, D., 2006. Multiconfiguration GPR measurements for geometric fracture characterization in limestone cliffs (Alps), *Geophysics,* **71**(3), B85-B92.

Jol, H.M. (ed.), 2008. *Ground Penetrating Radar Theory and Applications,* Elsevier, p. 524.

Kiefer, J., 1953. Sequential minimax search for a maximum, *Proc. Am. Math. Soc.,* **4**(3), 502–506.

Kilburn, R.J.C. & Voight, B., 1998. Slow rock fracture as eruption precursor at Soufriere Hills volcano, Montserrat, *Geophys. Res. Lett.,* **25**(19), 3665–3668.

Lai, H.M., Lau, Y.P. & Wong, W.H., 2002. Understanding wave characteristics via linear superposition of retarded fields, *Am. J. Phys.,* **70**(2), 173–179.

Lane, J.W., Buursink, M.L., Haeni, F.P. & Versteeg, R.J., 2000. Evaluation of ground-penetrating radar to detect free-phase hydrocarbons in fractured rocks—results of numerical modeling and physical experiments, *Groundwater,* **38**(6), 929–938.

Mandelbrot, B.B., 1982. *The Fractal Geometry of Nature,* WH Freedman and Co., p. 468.

Michalski, K.A. & Zheng, D., 1990. Electromagnetic scattering and radiation by surfaces of arbitrary shape in layered media. I. Theory, *IEEE Trans. Antennas Propag.,* **38**(3), 335–344.

Mukherjee, S. & Everett, M.E., 2011. 3D controlled-source electromagnetic edge-based finite element modeling of conductive and permeable heterogeneities, *Geophysics,* **76**(4), F215–F226.

National Research Council, Committee on Fracture Characterization and Fluid Flow, 1996. *Rock Fractures and Fluid Flow: Contemporary Understanding and Applications,* National Academies Press, p. 549.

Orfanidis, S.J., 2000. *Electromagnetic Waves and Antennas,* Rutgers University, p. 778.

Oron, A.P. & Berkowitz, B., 1998. Flow in rock fractures: the local cubic law assumption reexamined, *Water Resour. Res.,* **34**(11), 2811–2825.

Patriarca, C., Lambot, S., Mahmoudzadeh, M.R., Minet, J. & Slob, E., 2011. Reconstruction of sub-wavelength fractures and physical properties of masonry media using full-waveform inversion of proximal penetrating radar, *J. appl. Geophys.,* **74**(1), 26–37.

Pearce, J. & Mittleman, D., 2002. Defining the Fresnel zone for broadband radiation, *Phys. Rev. E,* **66**(5), doi:10.1103/PhysRevE.66.056602.

Purcell, E.M., 2011. *Electricity and Magnetism,* Cambridge Univ. Press, p. 484.

Russakoff, G., 1970. A derivation of the macroscopic Maxwell equations, *Am. J. Phys.,* **38**(10), 1188–1195.

Sambuelli, L. & Calzoni, C., 2010. Estimation of thin fracture aperture in a marble block by GPR sounding, *Boll. Geofis. Teor. Appl.,* **51**(2–3), 239–252.

Sassen, D.S. & Everett, M.E., 2009. 3D polarimetric GPR coherency attributes and full-waveform inversion of transmission data for characterizing fractured rock, *Geophysics,* **74**(3), J23–J34.

Shakas, A. & Linde, N., 2015. Effective modeling of ground penetrating radar in fractured media using analytic solutions for propagation, thin-bed interaction and dipolar scattering, *J. appl. Geophys.,* **116**, 206–214.

Shakas, A., Linde, N., Baron, L., Bochet, O., Bour, O. & Le Borgne, T., 2016. Hydrogeophysical characterization of transport processes in fractured rock by combining push-pull and single-hole ground penetrating radar experiments, *Water Resour. Res.,* **52,** 938–953.

Shepard, A.K., Bracket, R.A. & Arvidson, R.E., 1995. Self-affine (fractal) topography: surface parameterization and radar scattering, *J. geophys. Res.,* **100**(E6), 11 709–11 718.

Shubitidze, F., O'Neill, K., Haider, S.A., Sun, K. & Paulsen, K.D., 2002. Application of the method of auxiliary sources to the wide-band electromagnetic induction problem, *IEEE Trans. Geosci. Remote Sen.,* **40**(4), 928–942.

Taflove, A. & Hagness, S.C., 2000. *Computational Electrodynamics,* Artech House Publishers, p. 611.

Talley, J., Baker, G.S., Becker, M.W. & Beyrle, N., 2005. Four dimensional mapping of tracer channelization in subhorizontal bedrock fractures using surface ground penetrating radar, *Geophys. Res. Lett.,* **32**(4), L04401, doi:10.1029/2004GL021974.

Tsang, C.F., Neretnieks, I. & Tsang, Y., 2015. Hydrologic issues associated with nuclear waste repositories, *Water Resour. Res.,* **51,** 6923–6972.

Tsoflias, G.P. & Becker, M.W., 2008. Ground penetrating radar response to fracture-fluid salinity: why lower frequencies are favorable for resolving salinity changes, *Geophysics,* **73**(5), J25–J30.

Tsoflias, G.P. & Hoch, A., 2006. Investigating multi-polarization GPR wave transmission through thin layers: implications for vertical fracture characterization, *Geophys. Res. Lett.,* **33**(20), doi:10.1029/2006GL027788.

Tsoflias, G.P., Halihan, T. & Sharp, J.M., 2001. Monitoring pumping test response in a fractured aquifer using ground penetrating radar, *Water Resour. Res.,* **37**(5), 1221–1229.

Tsoflias, G.P., Van Gestel, J.P., Stoffa, P.L., Blankenship, D.D. & Sen, M., 2004. Vertical fracture detection by exploiting the polarization properties of ground penetrating radar signals, *Geophysics,* **69**(3), 803–810.

Tsoflias, G.P., Perll, C., Baker, M. & Becker, M.W., 2015. Cross-polarized GPR imaging of fracture flow channeling, *J. Earth Sci.,* **26**(6), 776–784.

Warren, C., Giannopoulos, A. & Giannakis, I., 2015. An advanced GPR modelling framework—the next generation of gprMax, in *Proc. 8th Int. Workshop Advanced Ground Penetrating Radar,* doi:10.1109/IWAGPR.2015.7292621.

Widess, M.B., 1973. How thin is a thin-bed?, *Geophysics,* **38**(6), 1176–1180.